

# Ultra-high electro-optic activity demonstrated in a silicon-organic hybrid modulator: supplementary material

CLEMENS KIENINGER,<sup>1,2,4</sup> YASAR KUTUVANTAVIDA,<sup>1,2</sup> DELWIN L. ELDER,<sup>3</sup> STEFAN WOLF,<sup>1</sup> HEINER ZWICKEL,<sup>1</sup> MATTHIAS BLAICHER,<sup>1</sup> JUNED N. KEMAL,<sup>1</sup> MATTHIAS LAUERMANN,<sup>1</sup> SEBASTIAN RANDEL,<sup>1</sup> WOLFGANG FREUDE,<sup>1</sup> LARRY R. DALTON,<sup>3</sup> AND CHRISTIAN KOOS<sup>1,2,\*</sup>

<sup>1</sup>Karlsruhe Institute of Technology (KIT), Institute of Photonics and Quantum Electronics (IPQ), 76131 Karlsruhe, Germany

<sup>2</sup>Karlsruhe Institute of Technology (KIT), Institute of Microstructure Technology (IMT), 76344 Eggenstein-Leopoldshafen, Germany

<sup>3</sup>University of Washington, Department of Chemistry, Seattle, Washington 98195, USA

<sup>4</sup>e-mail: clemens.kieninger@kit.edu

\*Corresponding author: [christian.koos@kit.edu](mailto:christian.koos@kit.edu)

Published 7 June 2018

This document provides supplementary information to “Ultra-high electro-optic activity demonstrated in a silicon-organic hybrid modulator,” <https://doi.org/10.1364/OPTICA.5.000739>. In the first part, the experimental setup for the  $\pi$ -voltage measurement of the SOH modulator is described. The second part includes a more detailed discussion of the on-chip losses of the modulator. The third part gives the mathematical relations that are used to link the measured  $U_\pi$  to the in-device EO figure of merit  $n^3r_{33}$  of the SOH modulator. In the fourth and fifth part we estimate the in-device EO coefficient and explain the corresponding error bounds for both  $r_{33}$  and  $n^3r_{33}$ . The last part discusses the EO material processing and the SOH functionalization.

## Experimental Setup for the $\pi$ -voltage measurement

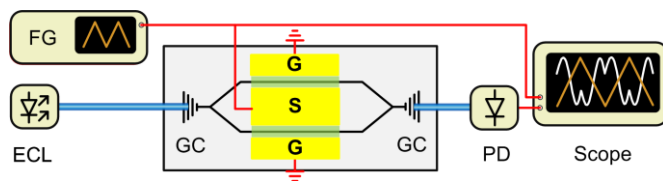


Fig.S1 Experimental setup for the  $\pi$ -voltage measurement. A triangular waveform obtained from a function generator (FG) is fed to the SOH modulator while an optical carrier obtained from an external cavity laser (ECL) is coupled to and from the chip via grating couplers (GC). The over-modulated optical signal is detected with a photodiode and an oscilloscope which also monitors the output of the FG.  $U_\pi$  can be read out as the voltage increment needed to drive the modulator from minimum to maximum transmission.

The experimental setup for the measurement of the  $\pi$ -voltage  $U_\pi$  of the silicon-organic hybrid (SOH) modulator is depicted in Fig. S1. The optical carrier obtained from an external cavity laser (ECL) is coupled to and from the silicon photonics chip via grating couplers

(GC) while a triangular waveform obtained from a function generator (FG) is fed to the SOH Mach-Zehnder Modulator (MZM) via microwave probes. The modulated light is detected with a photodiode that is connected to an oscilloscope. The oscilloscope additionally monitors the drive voltage applied to the MZM. The modulator is biased in its 3 dB point and the amplitude of the triangular waveform is chosen such that the modulator is over-modulated. That is, the peak-to-peak drive voltage is larger than the  $U_\pi$  of the device under test. In this case,  $U_\pi$  can be directly read out on the oscilloscope as the voltage increment needed to drive the modulator from its minimum to its maximum transmission point, see Fig. 2(c) and (d) of the main text.

## Optical loss of the SOH modulator

The total fiber-to-chip coupling losses amount to 8.9 dB caused by the non-ideal grating couplers. The on-chip loss of the MZM amounts to 8.2 dB. These on-chip losses can be decomposed into passive components and the loss in the SOH slot waveguide. The passive components include two multi-mode interference (MMI) couplers with losses of 0.37 dB per coupler, two optical mode

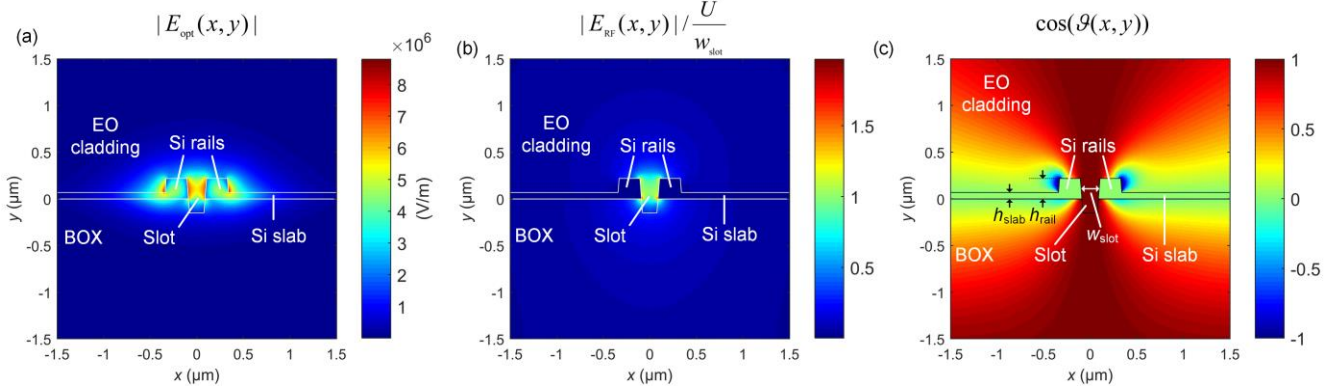


Fig. S2 Simulation results. (a) Magnitude of the optical field  $|E_{\text{opt}}(x, y)|$  for a launched optical power of 20 mW. (b) Normalized magnitude of the RF field,  $|E_{\text{RF}}(x, y)| / \frac{U}{w_{\text{slot}}}$  which amounts to about unity in the center of the slot, due to the normalization. Both optical and RF mode are tightly confined to the EO-material-filled slot region which results in efficient modulation. (c)  $\cos(\vartheta(x, y))$ , where  $\vartheta(x, y)$  is the angle between field lines of the optical and the RF mode. Inside, as well as above and below the slot region, field lines of optical and RF field are parallel resulting in  $\cos(\vartheta(x, y)) = 1$ . Directly above the slabs  $\cos(\vartheta(x, y))$  amounts to zero since the field lines are perpendicular. For all simulations we take into account that the slot is over-etched by 150 nm and we assume that the slot sidewalls are inclined by  $5^\circ$  with respect to the sample normal. We use two sets of devices in our work. They share the same slab height  $h_{\text{slab}}$  of 70 nm and silicon rail height  $h_{\text{rail}}$  of 220 nm but are different with respect to the slot width  $w_{\text{slot}}$  which is measured at half the silicon rail height and amounts to 190 nm and 150 nm, respectively.

converters at the strip-slot waveguide interfaces with losses of 0.20 dB per converter, and strip-waveguide propagation losses of 1.3 dB. The remaining 5.8 dB are attributed to the SOH slot waveguide propagation losses of the 1.5 mm long MZM which results in a propagation loss of 3.9 dB/mm. This includes both scattering loss from the slot waveguide sidewalls and free-carrier absorption loss in the doped silicon waveguide structures. Note that dedicated test structures were used to determine the grating coupler losses and the losses of the MMI couplers and the mode converter structures. The propagation losses of the strip waveguide amount to 2.5 dB/cm, specified by the chip manufacturer.

### Mathematical relations for calculating the in-device EO figure of merit $n^3 r_{33}$ of the SOH MZM

The phase change  $\Delta\phi$  of the optical carrier in the silicon-organic hybrid (SOH) modulator can be written as [1]

$$\Delta\phi = n^4 \frac{\epsilon_0 c \pi L}{2 \lambda P} \times \int_{-\infty}^{\infty} \int_{-\infty}^{\infty} r_{33}(x, y) E_{\text{RF}, \text{EO}}(x, y) |E_{\text{opt}, \text{EO}}(x, y)|^2 dx dy, \quad (\text{S1})$$

where  $n$  is the refractive index of the organic electro-optic (EO) material,  $\epsilon_0$  is the vacuum permittivity,  $c$  is the vacuum speed of light,  $L$  is the length of the modulator,  $\lambda$  is the wavelength of the optical carrier,  $r_{33}(x, y)$  is the non-uniform EO coefficient.  $E_{\text{RF}, \text{EO}}(x, y)$  is the component of the vectorial mode field of the applied radio frequency (RF) field pointing in the direction of the local chromophore orientation, which is defined by the axis of the molecular dipole. Similarly,  $E_{\text{opt}, \text{EO}}(x, y)$  is the corresponding component of the vectorial mode field of the optical carrier. The parameter  $P$  is the power of the optical mode, which is defined as

$$P = \frac{1}{2} \int_{-\infty}^{\infty} \int_{-\infty}^{\infty} \text{Re}\{\mathbf{E}_{\text{opt}}(x, y) \times \mathbf{H}_{\text{opt}}^*(x, y)\} \cdot \hat{e}_z dx dy. \quad (\text{S2})$$

The non-uniformity of  $r_{33}(x, y)$  is caused by the inhomogeneity of the electric poling field that dictates the local orientation of the chromophore dipoles. Due to this non-uniformity we consider here the mean value of the EO coefficient  $\overline{r_{33}}_{\text{slot}}$  in the slot region of the SOH modulator, i.e., the region between the Si rails. We furthermore assume a linear dependence of  $r_{33}$  on the poling field  $E_{\text{pol}}$  and approximate the  $(x, y)$ -dependency of the static poling field by the  $(x, y)$ -dependency of the RF mode field. This leads to

$$r_{33}(x, y) = \overline{r_{33}}_{\text{slot}} \frac{|E_{\text{pol}}(x, y)|}{|E_{\text{pol}}|_{\text{slot}}} \rho(x, y) \approx \overline{r_{33}}_{\text{slot}} \frac{|E_{\text{RF}}(x, y)|}{|E_{\text{RF}}|_{\text{slot}}} \rho(x, y), \quad (\text{S3})$$

where  $|E_{\text{pol}}|_{\text{slot}}$  and  $|E_{\text{RF}}|_{\text{slot}}$  are the mean values of the magnitude of the static poling field and the RF field in the slot region, respectively and  $\rho(x, y)$  is unity for  $(x, y)$ -values in the EO material and zero otherwise. By using Eq. (S3) we can rewrite Eq. (S1) as

$$\Delta\phi = n^4 \frac{\epsilon_0 c \pi L}{2 \lambda P} \overline{r_{33}}_{\text{slot}} \times \int_{-\infty}^{\infty} \int_{-\infty}^{\infty} \frac{|E_{\text{RF}}(x, y)|}{|E_{\text{RF}}|_{\text{slot}}} \rho(x, y) E_{\text{RF}, \text{EO}}(x, y) |E_{\text{opt}, \text{EO}}(x, y)|^2 dx dy. \quad (\text{S4})$$

Since the chromophore dipole moments align along the poling field (which is approximated by the RF field), the component  $E_{\text{RF}, \text{EO}}(x, y)$  is simply given by the magnitude of the RF field  $|E_{\text{RF}}(x, y)|$ . For the corresponding component of the optical mode we can deduce  $|E_{\text{opt}, \text{EO}}(x, y)| = |E_{\text{opt}}(x, y)| \cos(\vartheta(x, y))$ , where  $\vartheta(x, y)$  is the angle between field lines of the optical and the RF mode. Finally, we normalize the RF field by  $U/w_{\text{slot}}$ , where  $U$  is the RF voltage which is applied across the SOH slot waveguide and  $w_{\text{slot}}$  is the slot width measured at half the height of the silicon rails. Using these simplifications the induced phase change writes

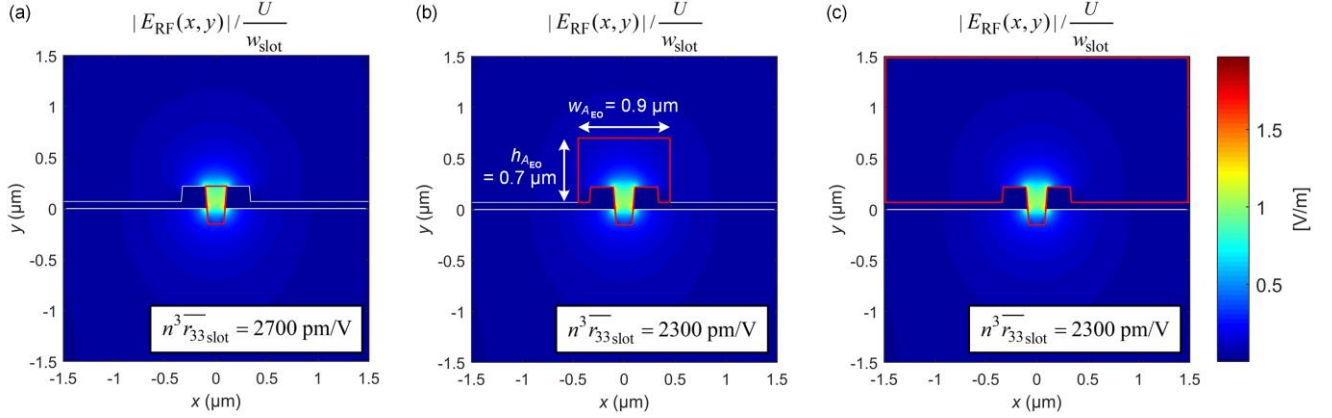


Fig.S3 Influence of choice of finite integration area  $A_{EO}$  on calculated  $n^3 \bar{r}_{33slot}$ . Depicted is the normalized magnitude of the RF field  $|E_{RF}(x, y)| / \frac{U}{w_{slot}}$  and different integration areas  $A_{EO}$  are indicated by red lines. (a) The integration area  $A_{EO}$  includes only the slot region and the over-etched volume. The corresponding  $n^3 \bar{r}_{33slot}$  would amount to 2700 pm/V, which overestimates the actual value. (b)  $n^3 \bar{r}_{33slot}$  decreases and converges to a constant value for growing  $A_{EO}$ . For an integration area of width and height of  $w_{AEO} = 0.9 \mu m$  and  $h_{AEO} = 0.7 \mu m$ , respectively, the limit of  $n^3 \bar{r}_{33slot} = 2300 \text{ pm/V}$  is reached. (c) Increasing the integration area over the whole displayed range doesn't influence the calculated  $n^3 \bar{r}_{33slot}$  any further.

$$\Delta\phi = n^4 \frac{\epsilon_0 c \pi L}{2 \lambda P} \bar{r}_{33slot} \frac{U}{w_{slot}} \times \int_{-\infty-\infty}^{\infty} \int_{-\infty-\infty}^{\infty} \frac{|E_{RF}(x, y)|^2 \rho(x, y)}{|E_{RF}|_{slot} U / w_{slot}} |E_{opt}(x, y)|^2 \cos^2(\vartheta(x, y)) dx dy. \quad (S5)$$

The SOH modulator is implemented as a Mach-Zehnder modulator (MZM) with a ground-signal-ground (GSG) transmission line configuration realizing push-pull operation. Therefore, for a total phase shift of  $\pi$ , the phase is shifted by only  $\pm\pi/2$  in the two arms of the MZM, respectively. As a consequence, the mean value of the EO figure of merit in the slot region  $n^3 \bar{r}_{33slot}$  is linked to the  $\pi$ -voltage  $U_\pi$  by

$$n^3 \bar{r}_{33slot} = \frac{\lambda w_{slot}}{2 U_\pi L} \times \left( \frac{\epsilon_0 c n}{2 P} \int_{-\infty-\infty}^{\infty} \int_{-\infty-\infty}^{\infty} \frac{|E_{RF}(x, y)|^2 \rho(x, y)}{|E_{RF}|_{slot} U / w_{slot}} |E_{opt}(x, y)|^2 \cos^2(\vartheta(x, y)) dx dy \right)^{-1} = \frac{\lambda w_{slot}}{2 U_\pi L} \times \frac{1}{\Gamma}, \quad (S6)$$

where we introduced the interaction factor  $\Gamma$ . The mode fields are simulated with the commercial software CST MICROWAVE STUDIO by using a finite integration method. The magnitude of the optical field for a launched power of 20 mW is depicted in Fig.S2(a). Fig.S2(b) shows the magnitude of the RF field at a frequency of 20 GHz normalized by  $U/w_{slot}$ . Since the electrical conductivity of the Si rails and slabs are much higher compared to the EO material and the lower SiO<sub>2</sub> cladding, these components are modeled as perfect electric conductors. Due to the normalization, the plotted field amounts to approximately unity in the slot region. In close proximity to the corners of the rails, values of about 2 are reached, which is hardly visible in the figure. It can be seen that both the RF and the optical mode are tightly confined in the slot region, which results in highly efficient modulation. Simulation results for  $\cos(\vartheta(x, y))$  are shown in Fig.S2(c). In the slot region as well as above and below the slot, field lines of RF and optical field are parallel resulting in  $\cos(\vartheta(x, y)) \approx 1$  whereas further left and

right of the slot  $\cos(\vartheta(x, y))$  decreases and becomes zero directly above and below the silicon slabs. Near the outer sidewalls of the rails, values of  $\cos(\vartheta(x, y)) \approx -1$  are found, since field lines of the optical and RF field are antiparallel in this region. With the simulated mode fields we can calculate the interaction factor  $\Gamma$ . Note that the slot dimensions, in particular the slot width  $w_{slot}$ , slightly influence the interaction factor. In Fig.S4 we plot the interaction factor  $\Gamma$  as a function of the slot width  $w_{slot}$ . It can be seen that  $\Gamma$  slightly decreases with increasing  $w_{slot}$ , due to the decreasing modal overlap of optical and RF mode.

Note that the slot of the presented SOH modulators is slightly over-etched, generating a free volume underneath the slot, as indicated in Fig.S2. This was confirmed by cutting a trench perpendicular to the direction of propagation of the slot waveguide by using focused ion beam (FIB) milling and by subsequently investigating the cross section of the waveguide. We extracted an over-etch depth of  $130 \pm 20 \text{ nm}$ . For our simulations, we assume that the volume caused by the over-etching is entirely filled with the organic EO material, and for all simulations we use an over-etch depth of 150 nm in order to not overestimate the calculated  $n^3 \bar{r}_{33slot}$ . Additionally, we consider in our model a silicon rail sidewall angle of  $5^\circ$  with respect to the wafer-normal direction. This value was obtained from transmission electron microscope (TEM) investigations of the cross section of similar SOH devices. In our simulations, we further use an increased density of mesh cells near the angled sidewall interfaces in order to better describe the inhomogeneity of the poling field in these regions.

The numerical evaluation of the integral in Eq. (S6), in praxis, requires the limitation to a finite integration area  $A_{EO}$  rather than an integration over the entire XY-plane. However,  $A_{EO}$  has to be carefully selected as  $n^3 \bar{r}_{33slot}$  is overestimated if  $A_{EO}$  is chosen too small.

In Fig.S3, the normalized magnitude of the RF field  $|E_{RF}(x, y)| / \frac{U}{w_{slot}}$  is depicted and three different integration areas  $A_{EO}$  are indicated by the red lines. In Fig.S3(a)  $A_{EO}$  extends only over the slot region and the over-etched region underneath the slot. Here, the calculated  $n^3 \bar{r}_{33slot}$  would amount to 2700 pm/V, which overestimates the actual value. This is due to the fact, that a



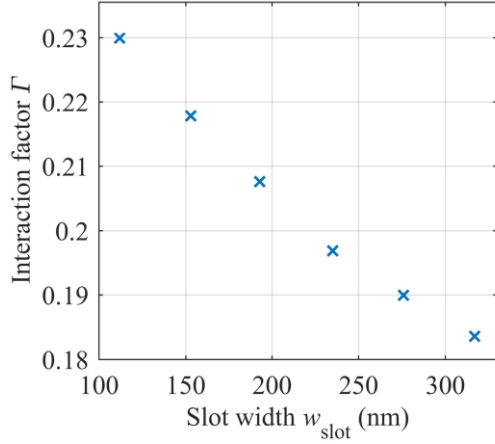


Fig. S4 Interaction factor  $\Gamma$  as a function of the slot width  $w_{\text{slot}}$  for an in-device refractive index of  $n = 1.81$ .  $\Gamma$  decreases with increasing slot width as the overlap between the optical and the RF mode decreases for wider slots.

considerable part of the RF and the optical mode are excluded from the chosen integration area  $A_{\text{EO}}$ . For growing integration area  $A_{\text{EO}}$ ,  $n^3 \overline{r_{33}}_{\text{slot}}$  decreases and converges to a constant value of 2300 pm/V. This value can be reached by only moderately extending  $A_{\text{EO}}$  with respect to the case shown in Fig. S3 (a), as illustrated in Fig. S3(b). Here, the integration area width and height amounts to  $w_{\text{AE0}} = 0.9 \mu\text{m}$  and  $h_{\text{AE0}} = 0.7 \mu\text{m}$ , respectively. In Fig. S3(c) the integration area is extended over the whole displayed range. However, the corresponding  $n^3 \overline{r_{33}}_{\text{slot}} = 2300 \text{ pm/V}$  does not change compared to the smaller integration area depicted in Fig. S3(b) since the contribution of the additionally included parts of the RF field and of the optical mode field is negligible.

For the remainder of the document as well as in the manuscript we avoid the inconvenient notation  $\overline{r_{33}}_{\text{slot}}$  for the mean in-device EO coefficient in the slot region. Instead, for the sake of readability, we simply refer to the in-device EO coefficient  $r_{33}$ . Note, however, that all reported values for  $n^3 r_{33}$  and  $r_{33}$  for JRD1 in the manuscript actually refer to  $n^3 \overline{r_{33}}_{\text{slot}}$  and  $\overline{r_{33}}_{\text{slot}}$ , respectively.

### Estimation of refractive index and in-device $r_{33}$

In principle, if the in-device refractive index  $n$  of the OEO material is known, the EO coefficient  $r_{33}$  can be calculated from the measured in-device EO figure of merit  $n^3 r_{33}$ . Quantifying the refractive index  $n$ , however, is a challenging task due to the inherent optical anisotropy of the OEO chromophores and the associated birefringence. The birefringence is caused by a local alignment of the chromophores, which may result from externally applied poling fields or from interactions of chromophores with adjacent surfaces. To estimate the refractive index of JRD1, we prepared unpoled and poled thin-film samples and directly measured the birefringence using variable-angle spectroscopic ellipsometry (VASE) [2]. The unpoled reference sample was fabricated by spin coating a roughly  $1 \mu\text{m}$  thick JRD1 film on an ITO-coated glass slide. Samples for poling are fabricated by additionally sputtering a thin film of gold on the JRD1 layer such that JRD1 is sandwiched between layers of ITO and gold, which serve as the two poling electrodes. Note that the poling field for our thin-film tests was limited to  $100 \text{ V}/\mu\text{m}$  by dielectric breakdown, which is smaller than the value of  $450 \text{ V}/\mu\text{m}$  used in SOH devices. For the VASE measurement, the gold top electrode is removed by

an etching step using an iodine ( $\text{I}_2$ )/potassium iodide (KI) solution after the poling process.

The ellipsometry data was acquired using a commercially available VASE ellipsometer (model M-2000 by J. A. Woollam Co.) [3]. For extracting the refractive indices from the raw data, we use the evaluation software supplied with the device (CompleteEASE software version 4.81) [4], modeling JRD1 as an anisotropic layer with refractive indices  $n_{\parallel}$  and  $n_{\perp}$  defined in the directions parallel and perpendicular to the sample surface, respectively. Note that the indices  $n_{\parallel}$  and  $n_{\perp}$  correspond to the coordinate system of the substrate on which the film is deposited and not to the index ellipsoid associated with an individual chromophore. The film indices  $n_{\parallel}$  and  $n_{\perp}$  are hence distinctively different from the ordinary and the extraordinary molecular refractive indices  $n_o$  and  $n_e$  of the chromophore. For the unpoled film we obtain  $n_{\parallel, \text{u}} = 1.85$ ,  $n_{\perp, \text{u}} = 1.76$  and  $\Delta n_{\text{u}} = n_{\perp, \text{u}} - n_{\parallel, \text{u}} = -0.09$ . Note that already the unpoled sample exhibits significant birefringence and that the refractive index  $n_{\parallel}$  in the in-plane direction exceeds the one measured in the surface-normal direction,  $n_{\parallel} > n_{\perp}$ . We attributed this phenomenon to chromophore-surface interactions, which favor orientation of chromophores parallel to the substrate surface, thus increasing  $n_{\parallel}$  and decreasing  $n_{\perp}$ . Upon poling, the birefringence reduces slightly and we obtain  $n_{\parallel, \text{p}} = 1.83$ ,  $n_{\perp, \text{p}} = 1.77$  and  $\Delta n_{\text{p}} = n_{\perp, \text{p}} - n_{\parallel, \text{p}} = -0.06$ . This change is attributed to an increased chromophore alignment perpendicular to the interface induced by the poling field. The comparison between unpoled and poled thin-film samples indicates that the birefringence induced by chromophore-surface interactions is of the same magnitude as the poling-induced birefringence.

For determining the EO coefficient  $r_{33}$  from the in-device EO figure of merit  $n^3 r_{33}$ , we need to know the in-device refractive index  $n = n_x$  seen by the dominant electric field ( $E_x$ ) of the optical quasi-TE mode, see Fig. S2 for a definition of the coordinate system. Since a direct measurement of the birefringence in the slot is not possible, we rely on an estimated value of  $n_x$ . In this context, it is important to avoid any underestimation of  $n_x$ , which would lead to an overestimation of  $r_{33}$ . The findings obtained from the characterization of birefringence in the thin film suggest that, after deposition, chromophores in SOH devices are predominantly aligned in the  $zy$ -plane, parallel to the slot sidewalls, forced by a strong influence of surface-chromophore interactions within the nanoscopic slot. In the slot, the influence of these interactions is even stronger than in our thin-film samples, and we hence expect an in-device refractive index  $n_x$  that does not exceed the value of  $n_{\perp, \text{u}} = 1.76$  measured in the unpoled thin film. Poling of the SOH modulator leads to a re-orientation of some of the chromophores along the  $x$ -direction, which would increase the refractive index again. However, this re-orientation only affects a rather small fraction of the overall number of chromophores – for our highest EO activity of  $n^3 r_{33} = 2300 \text{ pm/V}$ , the acentric order parameter amounts to  $\langle \cos^3(\theta) \rangle < 0.2$ . We may hence assume that the in-device refractive index  $n_x$  is still close to the value of  $n_{\perp, \text{p}} = 1.77$  measured in the poled thin film and does very likely not exceed the average value of  $n = \frac{1}{2} (n_{\parallel, \text{p}} + n_{\perp, \text{p}}) \approx 1.80$ , which agrees well with the previously published “isotropic” refractive index of JRD1 of  $n = 1.81$ , which was obtained from an ellipsometry measurement, in which JRD1 was modeled as an isotropic layer [5]. To calculate  $r_{33}$  we therefore use the value of  $n = 1.81$ , which simplifies the comparison with previously published EO coefficients of JRD1 [5].

Using the in-device EO figure of merit  $n^3 r_{33} = 2300 \text{ pm/V}$  and the estimated in-device refractive index of JRD1 of 1.81, we obtain  $r_{33} = 390 \text{ pm/V}$ . Note that this value has to be taken with caution, since the refractive index may still be subject to large uncertainties.

### Error estimation of in-device $r_{33}$ and $n^3r_{33}$

We identify the uncertainty of the slot width measurement and the uncertainty of the in-device refractive index as the two main reasons for errors in the reported values of  $r_{33}$  and  $n^3r_{33}$ . The slot widths were obtained by analyzing 70 top-view SEM micrographs for which we estimate a measurement accuracy of  $\Delta_w = \pm 10$  nm. The accuracy of the in-device refractive index we estimate to  $\Delta_n = \pm 0.1$ . Note that the inaccuracy in refractive index  $\Delta_n$  leads to an inaccuracy in the interaction factor  $\Gamma$ , see Equation S6. For the investigation of this effect, we plot the interaction factor  $\Gamma$  as a function of the refractive index  $n$  in Fig.S5. We can see that  $\Gamma$  increases with increasing  $n$ . Using the estimated value of  $n \approx 1.81$  as a reference, and assuming  $\Delta_n = \pm 0.1$ , we find for the interaction factor an error of  $\Delta_\Gamma = 0.011$ . Combining the above listed effects we obtain  $n^3r_{33} = (2300 \pm 170)$  pm/V and  $r_{33} = (390 \pm 70)$  pm/V for the error bounds of the in-device EO figure of merit and the in-device EO coefficient, respectively. The relative error for  $n^3r_{33}$  is smaller compared to the respective error of  $r_{33}$  since the uncertainty of the refractive index  $\Delta_n$  enters the calculation for the error of  $n^3r_{33}$  only indirectly via  $\Delta_\Gamma$  whereas both  $\Delta_n$  and  $\Delta_\Gamma$  have to be considered for the calculation of the uncertainty of  $r_{33}$ .

Note that the uncertainty in slot width  $\Delta_w = \pm 10$  nm induces an additional uncertainty of the interaction factor  $\Gamma$ , see Fig.S4. However, since the induced relative changes are about only 1 % we neglect this effect.

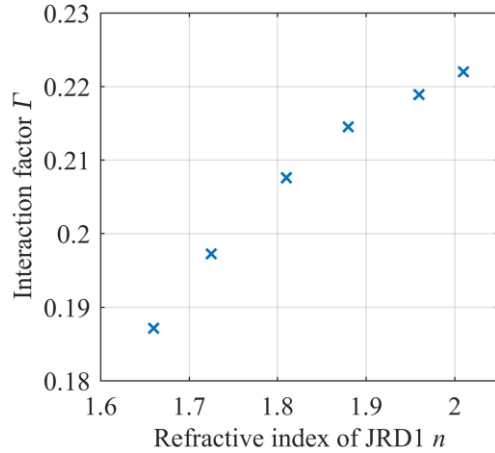


Fig.S5 Interaction factor  $\Gamma$  as a function of the refractive index  $n$  of JRD1 for a device with slot width of 190 nm. For a variation of the in-device refractive index of  $n = 1.81 \pm 0.1$ , the field interaction factor varies only by  $\Gamma = 0.208 \pm 0.011$ , corresponding to a relative change of 5 %.

### Material processing and device functionalization

For applying the JRD1 chromophore to the silicon chip, the organic material is first dissolved in 1,1,2-trichloroethane (TCE) and stirred for 3 hours to ensure good mixing. For material deposition on the silicon chip, we employ a micro dispenser setup consisting of a glass capillary with an inner tip diameter of 30  $\mu\text{m}$ . The position of the capillary can be adjusted by a computer controlled 3D translation stage. We rely on capillary forces to fill the needle with the solution. On touching the surface, the solution wets the chip over a limited region with a radius of about 15  $\mu\text{m}$ . For functionalizing the modulators, we translate the capillary along the Mach-Zehnder arms to obtain a uniform coverage of the silicon slot waveguides. For drying of the deposited solution, the chip is heated to 60  $^\circ\text{C}$  for 30 min. Subsequently, the device is stored in a

high vacuum ( $10^{-4}$  mbar) for 12 h at room temperature in order to remove the remaining solvent.

### References

1. C. Koos, *Nanophotonic Devices for Linear and Nonlinear Optical Signal Processing* (Univ.-Verl. Karlsruhe, 2007).
2. J. A. Woollam, B. D. Johs, C. M. Herzinger, J. N. Hilfiker, R. A. Synowicki, C. L. Bungay, "Overview of variable-angle spectroscopic ellipsometry (VASE): I. Basic theory and typical applications," *Proc. SPIE* 10294, Optical Metrology: A Critical Review, 1029402 (1999)
3. M-2000XI Spectroscopic Ellipsometer Hardware Manual, J. A. Woollam Co., Inc., 2010, [www.jawoollam.com](http://www.jawoollam.com)
4. CompleteEASE Data Analysis Manual, version 4.63, J. A. Woollam Co., Inc., 2011, [www.jawoollam.com](http://www.jawoollam.com)
5. W. Heni, C. Haffner, D. L. Elder, A. F. Tillack, Y. Fedoryshyn, R. Cottier, Y. Salamin, C. Hoessbacher, U. Koch, B. Cheng, B. Robinson, L. R. Dalton, and J. Leuthold, "Nonlinearities of organic electro-optic materials in nanoscale slots and implications for the optimum modulator design," *Opt. Express* **25**, 2627 (2017).